DOI 10.1007/s10946-021-09995-w
Journal of Russian Laser Research, Volume 42, Number 5, September, 2021

DESIGN AND TEMPERATURE SENSING PERFORMANCE OF A MODAL INTERFERENCE SENSOR WITH THE CORE MISMATCH-OFFSET STRUCTURE

Lijie Zhang,[1*] Yanling Xiong,[2] Naikui Ren,[2] Mingze Wu,[2] Rui Pan,[2] and Wenlong Yang[2]

[1] *College of Construction Engineering, Jilin University Changchun 130021, China*

[2] *College of Applied Science, Harbin University of Science and Technology Harbin 150080, China*

*Corresponding author e-mail: z82629049@163.com

Abstract

We design high-sensitive fiber-optic sensor based on modal interference for temperature measurements. The core mismatch-offset sensor is fabricated by splicing a section of multimode fiber (MMF) between two single-mode fiber (SMF) and offset splicing of SMF. We use the finite-difference beam propagation method to numerically analyze the mode and intensity distributions of the light field in the sensor. We optimize the structure parameters such as the length of MMF, the length of sensing SMF, and the offset of sensor; the optimum parameters of proposed sensor are 4.0 mm, 1.73 cm, and 3.5 μm, respectively. Experimental results show that the proposed sensor is successfully used to monitor the variation of ambient temperature, and it possesses a high temperature sensitivity of 167.2 pm/°C with good linearity. The core mismatch-offset sensor with high sensitivity and compact structure provides a new method for designing fiber-optic sensor and temperature sensing.

Keywords: temperature sensing, high sensitivity, modal interference, core mismatch splicing, offset splicing.

1. Introduction

Due to high sensitivity and flexible design, the fiber-optic sensor based on modal interference has attracted increasing attention in terms of weak signal detection, structural health monitoring of constructions, and deep sea detection. Design of modal interference sensor with new structure has been intensely developed in recent years.

Recently, many in-fiber Mach–Zehnder interferometer (MZI) sensors based on modal interference have been proposed for temperature [1], refractive index (RI) [2], curvature [3], and pressure monitoring [4]. There are several methods to fabricate the fiber-optic modal interference sensor such as tapering, splicing, long-period grating inscription, and partial collapsing of microholes [5–11]. Many modal interference sensors were proposed by splicing a section of the special fiber between two single-mode fibers (SMFs) such as multimode fiber (MMF), hollow core fiber, and multicore fiber [12–18]. Among them, the modal interference sensors with the SMF-MMF-SMF structure were widely used in fiber sensing applications. However, the temperature sensitivities of the sensors can only achieve about 115 pm/°C [19]. An optical fiber curvature sensor based on a twisted MMF sandwiched between two SMFs was proposed. When the temperature ranges from 21°C to 121°C, the sensitivity of the sensor is 10 pm/°C [20]. A simple fiber

Manuscript submitted by the authors in English on May 22, 2021.

sensor with the MMF-SMF-MMF structure was presented for the measurement of high temperatures. The temperature sensor can stably measure temperature up to more than 900°C with a sensitivity of 88 pm/°C [21]. Therefore, the temperature sensors based on modal interference remain great challenges in increasing the sensitivity.

In this work, we design a highly-sensitive core mismatch-offset sensor based on modal interference for temperature measurements. The core mismatch-offset sensor is fabricated by splicing a section of MMF between two SMF and offset splicing of SMF. The influence of the MMF length, sensing SMF length, and offset on the transmission spectra are numerically analyzed by the finite-difference beam propagation method, and the structure parameters of the sensor are optimized. The temperature sensing system is established to explore the temperature sensing properties of the sensor and to obtain a high temperature sensitivity of 167.2 pm/°C in the temperature range from 25°C to 40°C.

2. Principle of Sensing

The schematic diagram of the fiber-optic core mismatch-offset sensor is shown in Fig. 1. The core mismatch-offset sensor is fabricated by splicing a section of MMF between two SMF and offset splicing of SMF; see Fig. 1, where L_1 is the length of the MMF, L_2 is the length of the sensing SMF, and L_3 is the value of offset.

The light in the SMF is generated on the fundamental mode, and high-order modes can be excited while transmitting in MMF. The high-order modes transmit in the cladding of the sensing SMF, and the fundamental mode transmits in the core of the sensing SMF. Due to the offset splicing of SMF, the cladding mode and the core mode create interference due to the optical path difference of the offset.

Let us use the following notation. The mode in the core of SMF is the fundamental mode denoted as Lp_{01}. The distribution of light field is $E(r,0)$. The high-order modes Lp_{0n} (n is an integer) are linearly-polarized radial modes due to the circular symmetry of fiber. The distribution of the modal field is $F_m(r)$. Then we express the light field distribution as

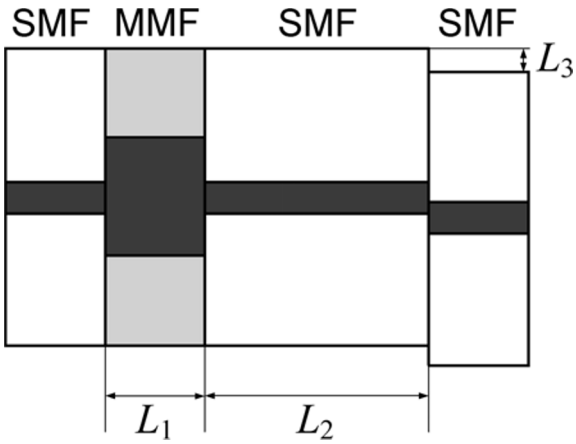

Fig. 1. Schematic diagram of the core mismatch-offset sensor.

$$E(r,0) = \sum_{m=1}^{M} C_m F_m(r), \tag{1}$$

where C_m is the excitation coefficient of the high-order modes; it reads

$$C_m = \frac{\int\limits_0^\infty E(r,0)F_m(r)r\,dr}{\int\limits_0^\infty F_m(r)F_m(r)r\,dr}. \tag{2}$$

The number of excited modes M can be approximated as follows:

$$M = \frac{V}{\pi} = \frac{2\pi}{\lambda} a\sqrt{n_{\text{co}}^2 - n_{\text{cl}}^2}\,, \tag{3}$$

where a is the radius of core in SMF, and n_{co} and n_{cl} are refractive indices (RIs) of the core and cladding in SMF, respectively. The light field distribution can be derived; it reads

$$E(r,z) = \sum C_m F_m(r) \exp(i\beta_m z), \tag{4}$$

where β_m is the propagation constant of the mode and z is the transmission distance in the MMF.

The high-order modes and fundamental mode create interference at the point of offset; it is described by the interference function

$$I(r) = E(r)E(r)^* = \sum_{m=1}^{M}\sum_{n=1}^{N} C_m C_n^* F_m(r) F_n(r) \exp[i(\beta_m - \beta_n)L]. \tag{5}$$

When high-order modes and fundamental mode satisfy the equality (N is integer)

$$(\beta_m - \beta_n)L = (2N+1)\pi, \tag{6}$$

the interference intensity achieves the minimum value. The characteristic wavelength can be derived; it is

$$\lambda = \frac{8a^2 n_{\text{co}}(2N+1)}{(m-n)(2m+2n-1)L_2}\,. \tag{7}$$

Therefore, the distance between interference peaks (valleys) can be expressed as [22]

$$\lambda_N - \lambda_{N-1} = \frac{16a^2 n_{\text{co}}}{(m-n)(2m+2n-1)L_2}\,. \tag{8}$$

One can see that the characteristic wavelength is related to the parameters such as the sensing SMF length L_2, the core radius, and the RI.

The phase difference ϕ between the core and cladding modes is

$$\phi = \frac{2\pi(n_{\text{co}}^{\text{eff}} - n_{\text{cl}}^{\text{eff}})}{\lambda} L_2 = \frac{2\pi}{\lambda}\Delta n^{\text{eff}} L_2, \tag{9}$$

where $n_{\text{co}}^{\text{eff}}$ is the effective RI of core and $n_{\text{cl}}^{\text{eff}}$ is the effective RI of cladding.

The free spectral range (FSR) reads

$$\text{FSR} = \frac{\lambda^2}{\Delta n^{\text{eff}} L_2}. \tag{10}$$

The wavelength shift $\Delta\lambda$ determined by Eqs. (7) and (8) is

$$\Delta\lambda = \frac{\text{FSR}\Delta\phi}{2\pi} = \frac{\lambda^2}{\Delta n^{\text{eff}} L_2}\frac{\Delta\phi}{2\pi}. \tag{11}$$

When the ambient temperature ΔT changes, the RI and length of the fiber vary with temperature, and the phase difference $\Delta\phi$ changes as

$$\Delta\phi = \frac{2\pi}{\lambda}\left[\Delta n^{\text{eff}}\Delta L_2 + \Delta(\Delta n^{\text{eff}})L_2\right] = \frac{2\pi}{\lambda} L_2 \Delta T\left[\Delta n^{\text{eff}}\alpha + (\xi_{\text{co}} n_{\text{co}}^{\text{eff}} - \xi_{\text{cl}} n_{\text{cl}}^{\text{eff}})\right], \tag{12}$$

where α is the thermal expansion coefficient of the fiber, and ξ_{co} and ξ_{cl} are the thermo-optic coefficient (TOC) of the core and cladding, respectively. Substituting Eq. (12) into Eq. (11), we arrive at

$$\Delta\lambda = \frac{\mathrm{FSR}}{2\pi} = \frac{\lambda^2}{\Delta n^{\mathrm{eff}} L_2}\frac{\Delta\phi}{2\pi} = \Delta T\lambda\left[\alpha + \frac{\xi_{\mathrm{co}} n_{\mathrm{co}}^{\mathrm{eff}} - \xi_{\mathrm{cl}} n_{\mathrm{cl}}^{\mathrm{eff}}}{\Delta n^{\mathrm{eff}}}\right]. \tag{13}$$

The temperature sensitivity of the sensor can be expressed as

$$\frac{\Delta\lambda}{\Delta T} = \lambda\left[\alpha + \frac{\xi_{\mathrm{co}} n_{\mathrm{co}}^{\mathrm{eff}} - \xi_{\mathrm{cl}} n_{\mathrm{cl}}^{\mathrm{eff}}}{\Delta n^{\mathrm{eff}}}\right]. \tag{14}$$

One can see that the temperature sensitivity of the sensor is related to α, ξ_{co}, ξ_{cl}, $n_{\mathrm{co}}^{\mathrm{eff}}$, and $n_{\mathrm{cl}}^{\mathrm{eff}}$. The TOC ξ_{co} and ξ_{cl} are determined by the material and the fiber mode. In some experiments, the TOC of the mode is approximately replaced by the TOC of the material. The approximation is beneficial to simplify the calculation of the fundamental mode and low-order modes, but it provides a large error in the calculation of high-order modes. In this work, we consider the difference between the mode TOC and the material TOC, with the mode TOC being regarded as the effective TOC. The TOC of the fundamental mode is similar to the TOC of the core in fiber, while the effective TOCs of the high-order modes in the cladding vary with the mode order. Therefore, the temperature sensitivity is related to the structural parameters of the sensor such as the length of MMF, the length of sensing SMF, and the value of offset. High temperature sensitivity can be obtained by optimizing structural parameters of the sensor.

3. Numerical Analysis

The intensity distributions of six modes in the sensor are shown in Fig. 2. The effective RIs of the six modes are 1.447372, 1.444654, 1.444483, 1.444179, 1.441757, and 1.444566, respectively.

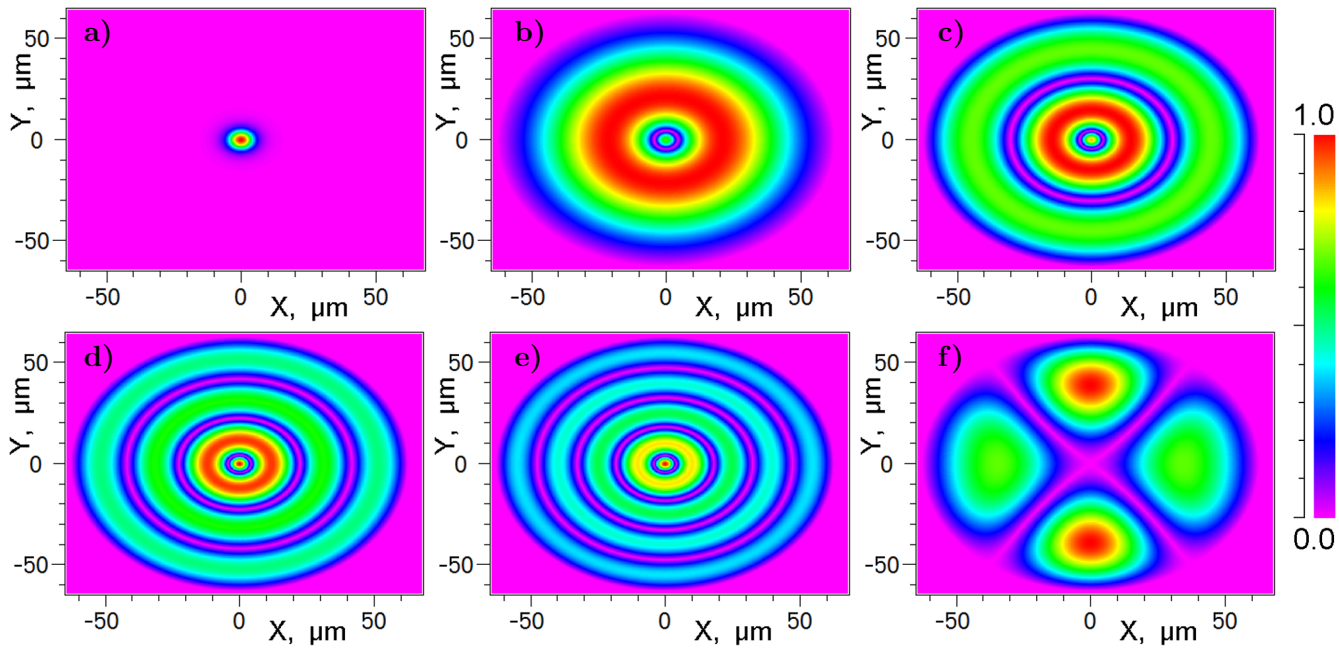

Fig. 2. Intensity distributions of modes in the sensor Lp_{01} (a), Lp_{02} (b), Lp_{03} (c), Lp_{04} (d), Lp_{05} (e), and Lp_{21} (f).

Ratios of the mode intensity to the total intensity vary with structural parameters of the sensor. As shown in Fig. 3, in the lead-in SMF, Lp_{01} is the primary mode, which is about 70% of the total intensity. The higher-order modes are excited in the MMF, the intensity ratio of Lp_{01} is reduced from 70% to 17%, and the intensity ratios of Lp_{02}, Lp_{03}, Lp_{04}, and Lp_{05} are 27%, 29%, 13%, and 7%, respectively. The intensity of Lp_{21} remains at a low level, and it can be ignored.

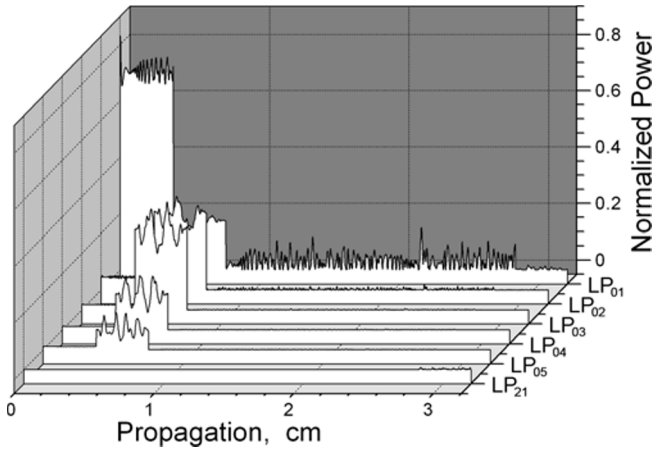

Fig. 3. Intensity of modes in the sensor elaborated.

The finite-difference beam propagation method is used to numerically analyze the mode and intensity distributions of the sensor and the effect of the MMF length L_1, sensing SMF length L_2, and offset L_3 on the transmission spectra of the sensor. The transmission spectra of sensors with L_2 ranged from 2.00 to 2.10 cm are shown in Fig. 4.

The relation between the sensing SMF length L_2 and the transmission intensity is shown in Fig. 4 a; here, the transmission intensity of different wavelengths varies with L_2. The transmission spectra of the sensor with different L_2 are shown in Fig. 4 b. Comparing the transmission spectra, we see that the transmission spectrum of the sensor with $L_2 = 2.07$ cm is symmetrical with respect to the interference valley, which is in accordance with the interference function; here, the wavelength of the interference valley is around 1543.7 nm.

Since the high-order modes are excited in the MMF, we studied the effect of the MMF length L_1 (at $L_2 = 2.07$ cm) on the transmission spectra. The relation between the MMF length L_1 and the transmission intensity is shown in Fig. 5 a, where there exists a distinct interference valley in the transmission spectrum of the sensor with $L_1 = 4$ mm at a wavelength of 1555 nm. In order to determine the value of L_1, we set the range of L_1 from 3.0 to 6.0 mm. The transmission spectra of the sensors are shown in Fig. 5 b. There are two obvious interference valleys in the transmission spectrum of the sensor with $L_1 = 3.8$ mm, and the corresponding wavelengths are 1527 and 1552 nm, respectively.

The value of offset L_3 has a great influence on the fringe visibility of the transmission spectra. The transmission intensity of the sensor with L_3 ranged from 0.0 to 18.0 μm (at $L_1 = 3.8$ mm and $L_2 = 2.07$ cm) is shown in Fig. 6. There are three interference valleys in the transmission spectrum. In order to determine the value L_3, the transmission spectra of the sensor with L_3 equal to 4.0 and 17.0 μm are analyzed. The relation between the offset L_3 and the wavelength transmission spectra are shown in Fig. 7, where the offset L_3 is equal to 4.0 and 17.0 μm, respectively.

As one can see in Fig. 7, the shift of the transmission spectra is related to the change in offset L_3; the fringe visibility increases with increase in offset L_3. There are two interference valleys in the spectra of the sensor with $L_3 = 4.0$ μm. Compared with the transmission spectrum of the sensor with $L_3 = 17.0$ μm, the transmission spectra of the sensor with $L_3 = 4.0$ μm are more conform to the modal interference function. Therefore, the structure parameters of the sensor were optimized. The optimum MMF length, sensitive SMF length, and offset of the sensor elaborated are 3.8 mm, 2.07 cm, and 4 μm, respectively.

We investigated the relation between the effective TOC and temperature sensitivity of the sensor by tracing the wavelength shifts of the transmission spectra. The TOC of the fiber core is $6.7 \cdot 10^{-6}/^{\circ}$C, which is similar to the TOC of the fundamental mode, while the effective TOC of the high-order mode

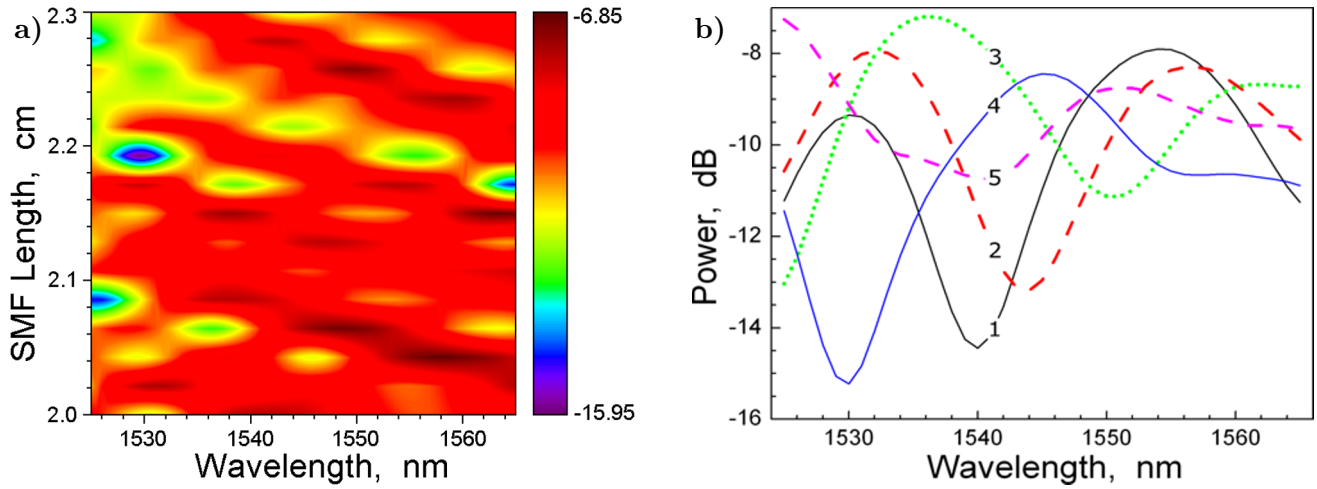

Fig. 4. The relation between the sensing SMF length L_2 and the transmission intensity (a) and the transmission spectra of the sensor with different L_2 (b). Here, curves 1–5 correspond to L_2 = 2.070, 2.074, 2.089, 2.091, and 2.100 cm.

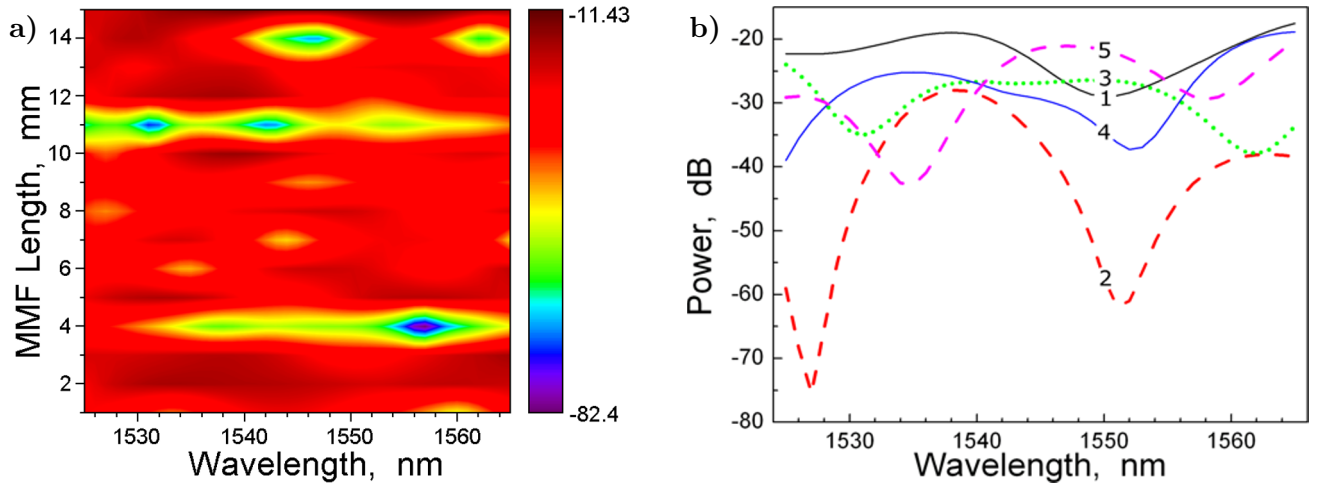

Fig. 5. The relation between the MMF length L_1 and the transmission intensity (a) and the transmission spectra of the sensor with different L_1 (b). Here, curves 1–5 correspond to L_2 = 3.00, 3.75, 4.50, 5.25, and 6.00 mm.

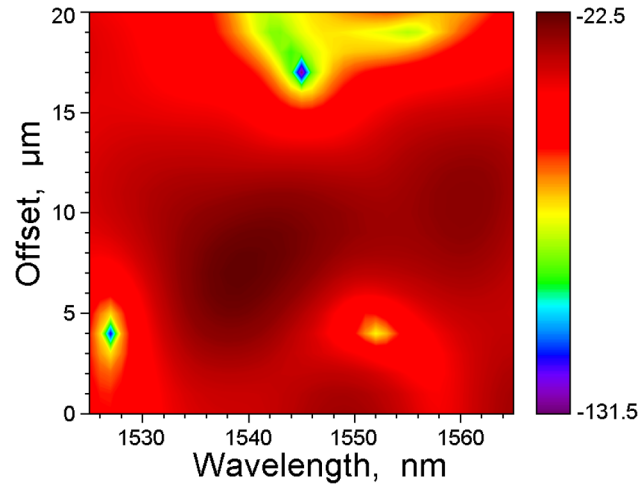

Fig. 6. The relation between the offset L_3 and the transmission intensity in the sensor elaborated.

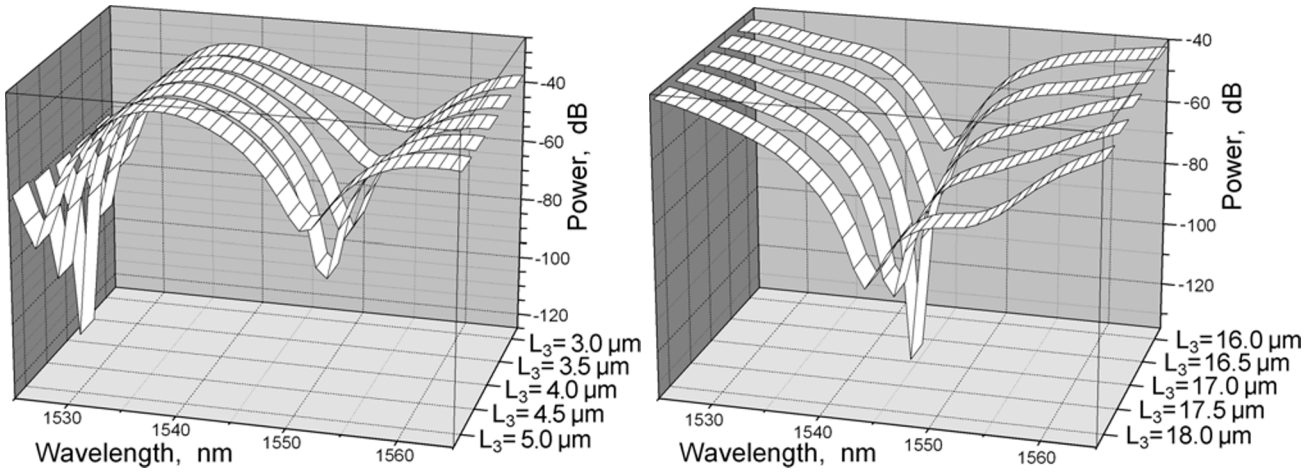

Fig. 7. The relation between the offset L_3 and the transmission spectra; here $L_3 = 3-5$ μm (left panel) and $L_3 = 16-18$ μm (right panel).

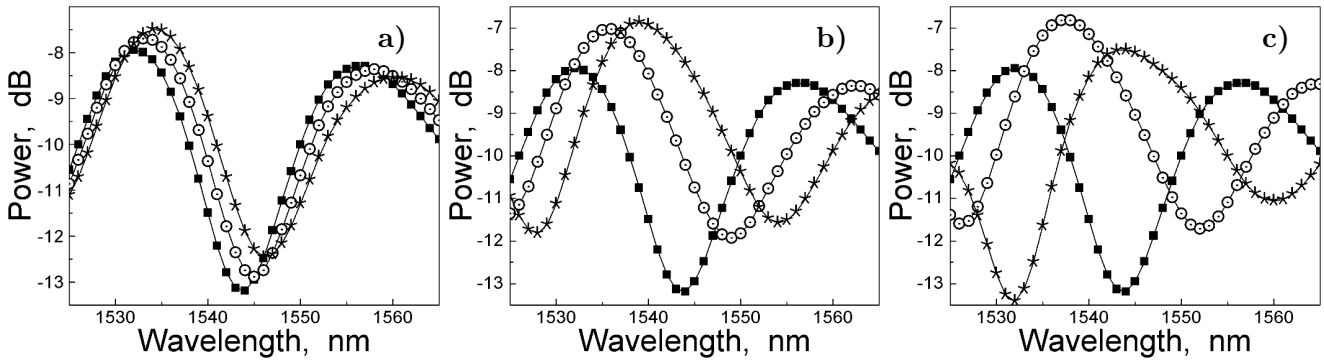

Fig. 8. The shift of the transmission spectra with different effective TOC $= 6.57 \cdot 10^{-6}/°\mathrm{C}$ (a), $6 \cdot 10^{-6}/°\mathrm{C}$ (b), and $5.56 \cdot 10^{-6}/°\mathrm{C}$ (c). Here, $T = 25°\mathrm{C}$ (■), $T = 75°\mathrm{C}$ (⊙), and $T = 125°\mathrm{C}$ (⋆).

in the cladding is different from the TOCs of the cladding materials.

The shifts of the transmission spectra with different effective TOC are shown in Fig. 8. The effective TOCs of cladding are $6.57{\cdot}10^{-6}/°\mathrm{C}$, $6{\cdot}10^{-6}/°\mathrm{C}$, and $5.56 \cdot 10^{-6}/°\mathrm{C}$, respectively, when the temperature ranged from 25°C to 125°C. In Fig. 8, we show the temperature sensitivity of the sensors with different effective TOC$= 6.57 \cdot 10^{-6}/°\mathrm{C}$, $6 \cdot 10^{-6}/°\mathrm{C}$, and $5.56 \cdot 10^{-6}/°\mathrm{C}$; they are 20 pm/°C, 100 pm/°C, and 160 pm/°C, respectively.

In order to investigate the relation between the effective TOC and temperature sensitivity, we analyzed the shifts of the transmission spectra; see Fig. 8. The relation between the effective TOC and temperature sensitivity is shown in Fig. 9.

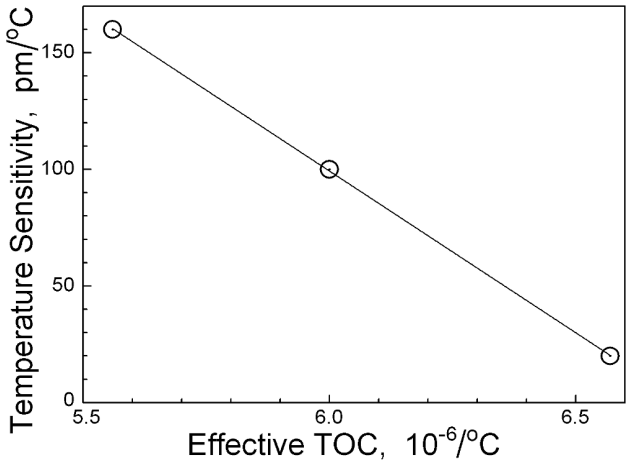

Fig. 9. The relation between the effective TOC and temperature sensitivity.

As one can see in Fig. 9, the temperature sensitivity of the sensor increases with decrease of the cladding effective TOC. Therefore, the temperature sensitivity of the sensor can be improved by changing the TOC difference between the core and cladding, which is consistent with the conclusion of Eq. (14).

4. Experiment

We fabricated the core mismatch-offset sensor by splicing a section of MMF between two SMF and offset splicing of SMF. The fibers used in the process of fabrication were SMF (9/125 μm) and MMF (105/125 μm), respectively. The MMF length equal to 5.0 mm, the sensing SMF length equal to 2.20 cm, and offset of 5.0 μm were determined according to the analysis results. As one can see in Fig. 10, the temperature sensing system in the experiment consists of four parts. There are amplified spontaneous emission (ASE) source, heating temperature platform, temperature sensor, and optical spectrum analyzer (OSA). The broadband laser light is generated from the ASE source and transmitted to the OSA through the temperature sensor. The heating platform displays and controls the temperature in the sensing region, and the temperature sensor is fixed on the heating platform to measure small changes of ambient temperature. The interference spectrum is received by the OSA with a resolution of 0.02 nm. The temperature is varied from 30°C to 55°C in a step of 5°C.

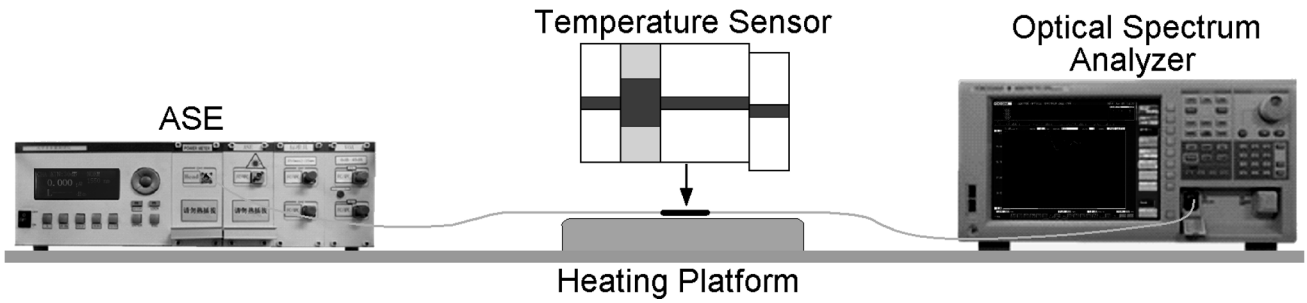

Fig. 10. Schematic diagram of monitoring temperature system.

The transmission spectra of the sensor at different temperatures are shown in Fig. 11.

One can see that the valley wavelength of transmission spectrum moves toward the long wavelength with temperature increase from 30°C to 55°C, and the wavelength of the interference valley is near 1552.5 nm. We demonstrated that the transmission spectra of the sensor experienced a red shift with increase in temperature. According to Eq. (7), we calculated that the valley wavelength of the interference between Lp_{01} and Lp_{02} was 1553.2 nm, and the valley wavelength of the interference between Lp_{01} and Lp_{05} was 1554.3 nm. The wavelength of the interference valley in the experiment was 1552.5 nm, which is close to 1553.2 nm. We obtained that the interference between the Lp_{01} mode and the Lp_{02} mode was the main part of the modal interference.

In order to investigate the temperature sensing properties of sensor, we analyzed the transmission spectra in Fig. 11. The experimental temperature varied from 30°C to 57°C. The relation between temperature variations and valley wavelength shifts is shown in Fig. 12.

The wavelength shift and temperature variation possesses a linear relationship, which reads

$$\lambda = 0.06065\,T + 1551.04517\,R^2 = 0.98011. \tag{15}$$

The temperature sensitivity of the sensor was 60.65 pm/°C.

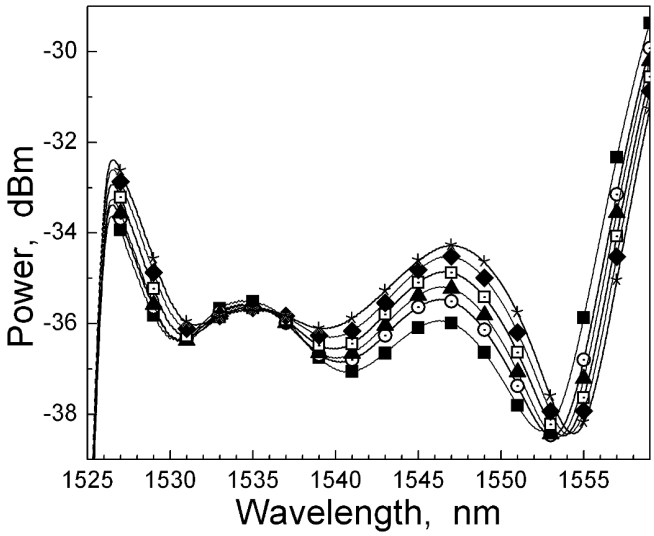

Fig. 11. The transmission spectra of the sensor at different temperatures equal to 30°C (■), 35°C (⊙), 40°C (▲), 45°C (⊡), 50°C (♦), and 55°C (⋆).

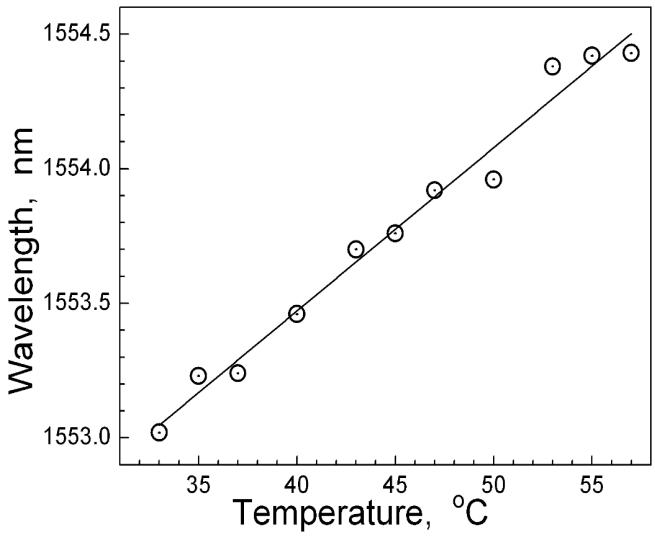

Fig. 12. The relation between temperature variations and valley wavelength shifts.

In order to improve the temperature sensitivity of the sensor, the structure parameters of sensor were optimized. The sensor with the MMF length equal to 4.0 mm, sensing SMF length equal to 1.73 cm, and offset of 3.5 μm was fabricated for temperature measurements. The transmission spectra of the optimized sensor at different temperatures are shown in Fig. 13.

One can see that the valley wavelength of transmission spectra moves toward the long wavelength with temperature increase from 25°C to 55°C; the wavelength of the interference valley is near 1531 nm. We demonstrated that the transmission spectra of the sensor experienced a red shift with increase in temperature. In view of Eq. (7), we calculate that the valley wavelength of the interference between Lp_{02} and Lp_{05} is 1527.5 nm and the valley wavelength of the interference between Lp_{03} and the Lp_{05} is 1539.7 nm. The wavelength of the interference valley in the experiment was 1531 nm, which is close to 1527.5 nm. We conclude that the interference between Lp_{02} mode and Lp_{05} is the main part of the modal interference.

In order to investigate the temperature sensitivity of optimized sensor, we analyzed the transmission spectra in Fig. 13. The experiment temperature varied from 25°C to 40°C. The relation between the temperature variation and the valley wavelength shift is shown in Fig. 14.

The wavelength shift and temperature variation possesses a linear relationship, and the relationship between temperature and wavelength reads

$$\lambda = 0.16720\,T + 1527.036\,R^2 = 0.98011. \tag{16}$$

One can conclude that the temperature sensitivity of the optimized sensor is 167.20 pm/°C at the wavelength equal to 1531 nm with the temperature ranging from 25°C to 40°C.

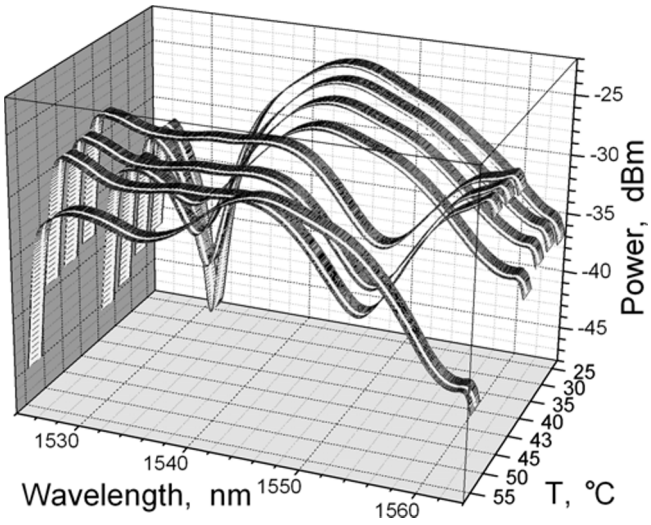

Fig. 13. The transmission spectra of the optimized sensor at different temperatures.

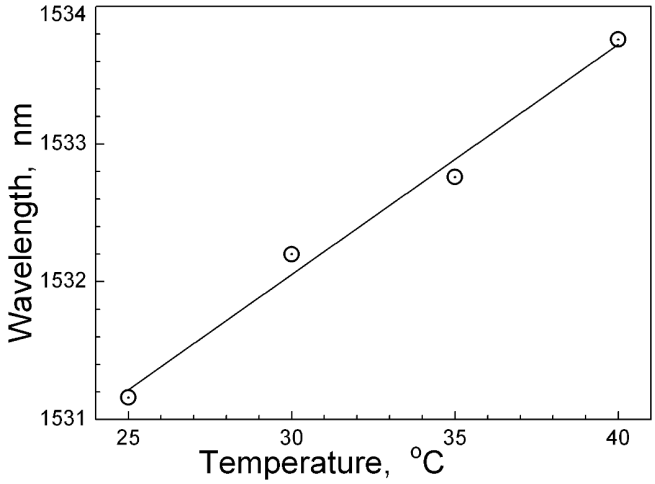

Fig. 14. The relation between the temperature variation and the valley wavelength shift.

5. Conclusions

We designed a core mismatch-offset sensor based on the modal interference for temperature measurements. We numerically analyzed the influence of the MMF length, sensing SMF length, and offset on the transmission spectra by the finite-difference beam propagation method and optimized the structure parameters of the sensor. The optimum MMF length, sensing SMF length, and offset parameters of the sensor elaborated are 4.0 mm, 1.73 cm, and 3.5 μm, respectively. We established the temperature sensing system to investigate the temperature sensitivity of the sensor elaborated. Experimental results showed that the interference between Lp_{02} mode and Lp_{05} mode corresponded to the main modal interference of the sensor. The sensor elaborated provides a high temperature sensitivity of 167.2 pm/°C at 1531 nm with the temperature ranging from 25°C to 40°C, which demonstrates higher sensitivity compared to conventional modal interference sensors.

Acknowledgments

This work was financially supported by the National Key R&D Program of China No. 2019YFC1804802, the Natural Science Foundation of Heilongjiang Province Nos. YQ2019A004 and LH2019F022, and the National Science Foundation for Postdoctoral Scientists of Heilongjiang Province No. LBH-Z19070.

References

1. Y. Y. Xiao, X. P. Cai, and H. Chen, *Optik*, **191**, 116 (2019).
2. X. Liu, Y. Zhao, R. Q. Lv, et al., *IEEE Photon. Technol. Lett.*, **28**, 13 (2016).
3. Y. Gong, T. Zhao, Y. J. Rao, et al., *IEEE Photon. Technol. Lett.*, **23**, 11 (2011).
4. Y. Zhao, Q. Wu, and Y. Zhang, *Measurement*, **148**, 106792 (2019).
5. M. Chen, Y. Zhao, H. Wei, et al., *Opt. Fiber Technol.*, **53**, 102025 (2019).
6. Q. Zhou, J. Li, and L. Chen, *IEEE Photon. Technol. Lett.*, **27**, 1849 (2015).

7. W. Huang, Y. Liu, and Z. Wang, *Appl. Opt.*, **54**, 285 (2015).
8. Y. Yu, Y. Zhang, and Z. Ou, *Photonic Sens.*, **5**, 376 (2015).
9. J. H. Liou and C. P. Yu, *Opt. Express*, **23**, 6946 (2015).
10. X. Dong, H. Du, X. Sun, et al., *Sensors*, **18**, 1549 (2018).
11. X. Zhang, Y. Liu, Z. Wang, et al., *Opt. Express*, **26**, 7013 (2018).
12. S. Mikroulis, M. P. Thakur, J. E. Mitchell, *IEEE Photon. Technol. Lett.*, **28**, 4 (2016).
13. E. Li, X. Wang, and C. Zhang, *Appl. Phys. Lett.*, **89**, 9 (2006).
14. D. P. Hand, F. Yu, J. C. Knight, et al., *Opt. Express*, **25**, 17 (2017).
15. J. E. Antonio-Lopez, Z. S. Eznaveh, P. Li Kam Wa, et al., *Opt. Lett.*, **39**, 15 (2014).
16. R. Kose, K. Yamaguchi, and T. Okayama, *Cellulose*, **23**, 2 (2016).
17. Y. Liu, W. Peng, X. Zhang, et al., *Opt. Commun.*, **319**, 106 (2014).
18. M. Shao, L. Han, H. Sun, et al., *Opt. Commun.*, **453**, 124356 (2019).
19. Y. Zhao, L. Cai, X. G. Li, *IEEE T. Instrum. Meas.*, **66**, 1 (2017).
20. K. Tian, Y. Xin, W. Yang, et al., *J. Lightw. Technol.*, **35**, 9 (2017).
21. L. V. Nguyen, D. Hwang, S. Moon, et al., *Opt. Express*, **16**, 15 (2008).
22. Y. Gong, T. Zhao, Y. J. Rao, et al., *IEEE Photon. Technol. Lett.*, **23**, 11 (2011).